Article

Surface persistence of trace level deposits of highly energetic materials

Leonardo C. Pacheco-Londoño [1,2,*] , **Jose L. Ruiz-Caballero**[1,3] , **Michael L. Ramirez-Cedeño**[1],
Ricardo Infante-Castillo[4] , **Nataly J. Galan-Freyle**[1,2] and **Samuel P. Hernandez-Rivera** [1,*]

[1]   Affiliation 1; R3-C Research and Education Component of ALERT DHS Center of Excellence for Explosives Research, Department of Chemistry, University of Puerto Rico, Mayaguez Campus, Mayaguez, PR 00681, USA.

[2]   Affiliation 2; School of Basic and Biomedical Sciences, Universidad Simon Bolivar, Barranquilla, Colombia.

[3]   Affiliation 2; Joseph Smith & Sons Inc, Capitol Heights, MD, USA.

[4]   Affiliation 2; Department of Physics-Chemistry, University of Puerto Rico, Arecibo, PR 00614, USA.

*   Correspondence: leonardo.pacheco@unisimonbolivar.edu.co, Tel.: +573046489549 (L.P.); samuel.hernandez3@upr.edu (S.H.)

Abstract: The sublimation enthalpies ($\Delta_{sub}H$) of four highly energetic materials (HEMs): triacetone triperoxide (TATP), 2,4-dinitrotoluene (DNT), 2,4,6-trinitrotoluene (TNT) and 1,3,5-trinitrohexahydro-s-triazine (RDX) deposited on stainless steel (SS) substrates were determined by optical fibre coupled-grazing angle probe (GAP) FTIR spectroscopy and thermogravimetric analysis (TGA) for bulk crystaline HEMs samples. The desorption energy ($\Delta_{des}U$) of RDX on SS was also studied using grazing angle FTIR microscopy. Metastable phases of 2,4-DNT and TNT were observed when deposited on SS, and their $\Delta_{sub}H$ values were obtained by GAP measurements and compared with those for the crystalline phases. $\Delta_{sub}H$ for the α phase RDX was also determined by TGA measurements. A layer of crystalline β phase RDX was observed on SS, and it's $\Delta_{sub}H$ was determinate by GAP. PLS calibration curves for the surface concentrations of RDX on SS were generated using GAP to determinate the surface concentration with time at different temperatures.

Keywords: Sublimation, Explosive, FTIR, Thermogravimetric analysis, grazing angle

1. Introduction

The residence time of a highly energetic material (HEM) on a surface can be defined as the time that the material persists on the surface after its deposition. The concept is essential for the development of samples and standards for trace detection systems[1–12]. Aside from adhesion considerations, the residence time mainly depends on the vapor pressure of the compound and surface-HEM interactions. The vapor pressure of a HEM and its interaction with any given surface can be characterized in terms of the desorption energy and the sublimation enthalpy. The desorption energy ($\Delta_{des}U$) can be defined as the change in energy when a substance adsorbed on a surface is desorbed. The desorption of an adsorbed molecule is an elemental surface kinetics process and is a measure of the strength of the interaction between the surface and the adsorbed species[13]. The enthalpy of sublimation ($\Delta_{sub}H$) is the energy change when a compound changes from the solid phase to the gas phase. These enthalpies are present for a solid deposited on a surface. If the solid-surface interaction is small, $\Delta_{des}U$ is insignificant, and the sublimation is the main phenomenon. There are two general ways of calculating $\Delta_{sub}H$, i.e., directly and indirectly. In the direct method, a calorimeter is used to measure the heat exchanged during the change of phase. In the indirect determination, the vapor pressure, or a proportional parameter thereof, is measured at different temperatures and the

enthalpy can be calculated by use of the Clausius-Clapeyron equation.[14–16]. Various approaches can be taken to characterize the vapor pressures of materials. These include direct measurements with a manometer[17], the use of mass spectrometry to monitor the gas phase concentration of the species, measurement of sample volatilization by vacuum diffusion[18] (using a Knudsen cell), and boiling point determination under different pressures by differential scanning calorimetry.. Several studies have reported that thermogravimetric analysis (TGA) is a rapid and convenient method to obtain vapor pressure curves and the enthalpies of sublimation and vaporization of volatile materials such as active pharmaceutical ingredients and HEMs with different vapor pressures[19–22]. Sublimation enthalpies can also be measured by spectroscopic methods such as fluorescence. For example, Stefanov et al. used fluorescence monitoring to estimate the sublimation enthalpies of tetraphenylporphyrin, porphine, and Nile red, a fluorescent intracellular dye[23]. In the present study, the sublimation enthalpies of triacetone triperoxide (TATP), 2,4-dinitrotoluene (DNT), 2,4,6-trinitrotoluene (TNT), and 1,3,5-trinitrohexahydro-s-triazine (RDX) deposits on stainless steel (SS) substrates were obtained from mid-infrared (MIR) grazing angle probe fibre optic (GAP) coupled FTIR spectroscopy measurements, which were performed under isothermal conditions at different temperatures. The results were then compared with those obtained for the bulk samples by TGA. Furthermore, $\Delta_{des}U$ for RDX on SS was obtained by thermal desorption spectroscopy (TDS) measurements using grazing-angle objective (GAO) FTIR microspectroscopy.

2. Materials and Methods

2.1. Reagents

The reagents used in this research were acetone (CH_3COCH_3, 98%, Aldrich-Sigma Chemical Co., Milwaukee, WI), isopropanol (99%, Aldrich-Sigma) hydrogen peroxide (H_2O_2, 50% in water, Aldrich-Sigma), hydrochloric acid (HCl, 12 M, Merck, VWR, Inc., West Chester, PA), sulfuric acid (H_2SO_4, 18 M, Merck, VWR), and dichloromethane (CH_2Cl_2, Aldrich-Sigma). Standard solutions of RDX (1000 ppm in acetonitrile, GC/MS primary standards grade) were obtained from Restek Corp. (Bellefonte, PA) and from Chem Service, Inc., (West Chester, PA). Crystalline samples of 2,4-DNT and TNT were purchased from Chem Service, Inc., (West Chester, PA).

2.2. Synthesis of TATP

Caution: TATP is a primary explosive sensitive to impact, friction, electric discharge, and flame. The synthesis and handling of TATP are dangerous operations that require safety precautions. TATP could not be purchased from chemical suppliers at the level of purity and amount required for the study. Samples were prepared in small quantities as needed without storing due to the high thermal instability of this powerful and highly unstable explosive. For the synthesis, 1 mL of 0.01 M HCl was mixed with 3 mL of peroxide, 2 mL of acetone, and 4 mL water. Crystals formed after 5 h. The crystals were then filtered and washed, first with cold distilled water and next with a small amount of cold methanol. The solid was then recrystallized from methanol.

2.3. Instrumentation

A grazing angle probe (GAP; Remspec Corp., Charlton, MA) interfaced to a Vector-22 FTIR interferometer (Bruker Optics, Billerica, MA) equipped with an external mercury cadmium telluride (MCT) MIR detector was used for the spectroscopic monitoring of analytes deposited on the test surfaces. The GAP head uses carefully aligned mirrors to deliver a MIR beam to the sample surface at the grazing angle (approximately 80° from the surface normal).[24]. The spectrometer was coupled to the GAP by a MIR transmitting fiber optic cable[25,26]. The 1.5 m fiber was made from a chalcogenide (As-Se-Te) optical glass bundle that transmits throughout the MIR region except for a strong H-Se absorbance band at 2200 cm^{-1}. The GAP beam was focused on a solid surface that was in thermal

contact with an aluminum block equipped with a temperature controlled water bath. Samples were placed on SS plates on top of this surface. The experimental setup is illustrated in Fig.1.
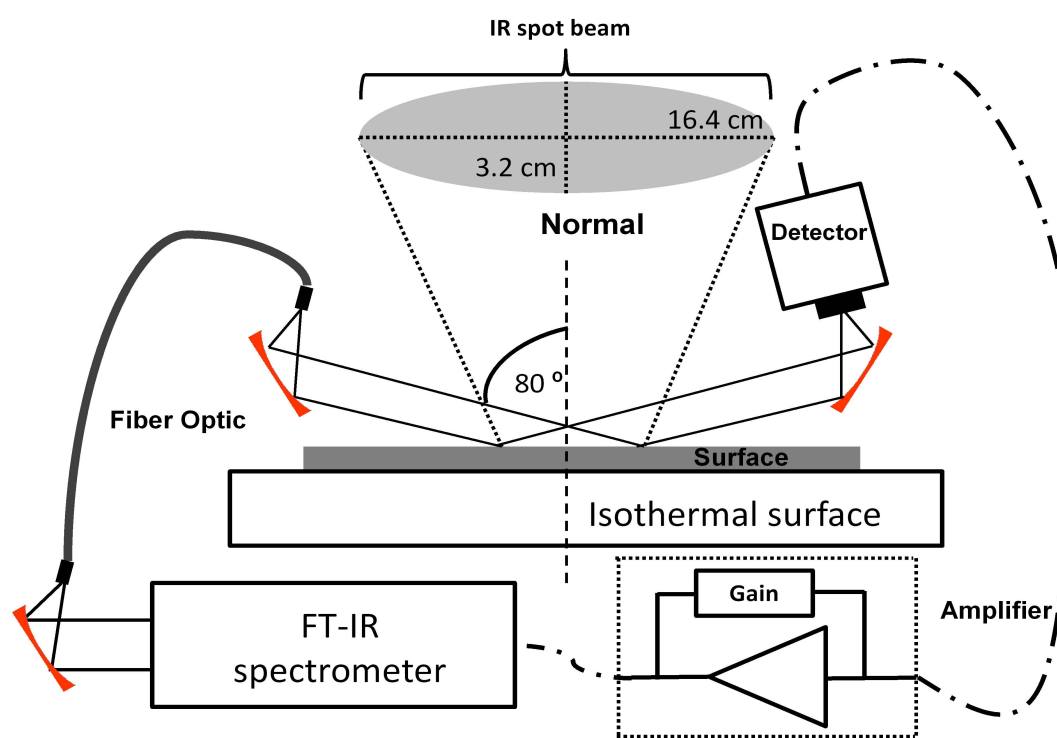

Figure 1. GAP experimental setup for the sublimation HEM.

The MIR beam was reflected in an elliptical shape from the metal surface. The size of the ellipse along the major axis was ≈16 cm and along the minor axis was ≈3 cm. The beam intensity pattern on the surface was well described by a Gaussian distribution. The behavior of the relative intensity (I_r) was measured and can be fitted as:

$$I_r = exp[-(0.10 \pm 0.01)x^2 - (3.3 \pm 0.2)y^2] \tag{1}$$

Rewriting the Eq.1

$$\left(\frac{x}{3.2}\right)^2 + \left(\frac{y}{0.6}\right)^2 = -ln(I_r) \tag{2}$$

This expression describes an ellipse with the major axis measuring 3.4 cm and the minor axis measuring 0.6 cm. These values for the axes represent an ellipse that contains 63.2 % of the infrared beam[27]. For 99% reflection of the MIR light on the surface, the ellipse had dimensions of 6.8 cm on the major axis and 1.2 cm on the minor axis Infrared microscopy in the MIR region was also used to characterize the samples. A Bruker Optics model, IFS 66v/S spectrometer, coupled to a Hyperion II IR microscope equipped with GAO was used. A computer-controlled motorized stage, a cryocooled MCT detector and a potassium bromide (KBr) beam splitter allowed sampling of areas with dimensions of 100×100 μm^2. TGA was done using a model Q-500 (TA Instruments, New Castle, DE, USA) for all bulk measurements. A constant ultra-high purity nitrogen flow was used to run the samples. Standard platinum sample holders were used. Aluminum pans on top of the platinum holders were used to contain the samples to a specific area. The TGA was temperature calibrated using the nickel Curie point (356°C) apparent weight loss according to manufacturer-optimized procedures.

2.4. Sublimation study by thermal analysis

TGA is a rapid and convenient method for obtaining vapor pressure curves and the enthalpies of sublimation and vaporization of volatile materials. However, TGA cannot be used for measuring the sublimation of thin layers because the limit of mass determination of a TGA apparatus is higher than the mass of a thin layer. For example, for a surface of 1 cm^2 that contains 0.1 μg/cm^2 of material, the total mass is 100 ng (0.1 μg), which is too low to be measured by the microbalance in a conventional TGA instrument[28]. TGA methods for measuring vapor pressure and sublimation enthalpies are based on the principle that sublimation, as well as evaporation, is a zero-order process. Thus, the mass loss under isothermal conditions must be constant[21,29]. The mathematical expression that correlates the vapor pressure originates from Langmuir's work of 1913[30]

$$\left(\frac{1}{area}\right)\left(\frac{dm}{dt}\right) = p\alpha_v \left(\frac{M}{2\pi R_g T}\right)^{0.5} \tag{3}$$

where $(1/area)(dm/dt)$ is the rate of mass loss per unit area (Kg $* $ s^{-1} $*$ m^{-2}), p is the vapor pressure (Pa), M is the molecular mass of the evaporating compound (kg$*$ mol^{-1}), R$_g$ is the gas constant (J$*$ K^{-1} $*$ mol^{-1}), T is the absolute temperature (K), and α_v is the vaporization coefficient. In a vacuum, α_v is assumed to be 1, but in a flowing gas such as that used in TGA experiments, α_v can have different values. Rearranging the Langmuir equation results in:

$$p = k_t v_s \tag{4}$$

where k$_t$=(1/area)((2πR$_g$)$^{0.5}$/α_v), and v_s=(dm/dt)(T/M)$^{0.5}$. If a compound is thermally stable and its vapor pressures at different temperatures are known, it is possible to correlate the vapor pressure to the mass-loss rates obtained by TGA from which k$_t$ is obtained[31]. This can be used to determine the vapor pressure of other substances. The study of the sublimation kinetics of HEMs by TGA involves determining the rate of mass loss at several isothermal points over the temperature range of interest. In the present study, the mass of the samples was monitored under isothermal conditions for a minimum of 30 min. The temperature range was different for each explosive at data intervals of 5 °C, 1 °C, and 0.5 °C. For TATP, the temperature range was 20-65 °C; for 2,4-DNT, the range was 25-70 °C; for TNT, the range was 30-90 °C; and for RDX, the range was 50-125 °C. To determine the vapor pressure, the rate of mass loss for benzoic acid was measured every 2 °C from 22 to 90 °C. The value of v_s was calculated, and the value of k$_t$ was obtained by fitting the vapor pressures in the literature[32,33].

2.5. Sublimation study by GAP

The sublimation of thin layers and trace amounts of HEMs was studied by FTIR-GAP. Samples were prepared by depositing the HEMs from liquid solutions, generating homogeneous distributions on the surfaces of the SS substrates after drying at room temperature. The morphologies of the residues of the HEMs on the SS surfaces were terraces for TATP, droplets for 2,4-DNT and TNT, and layers for RDX, as determined using optical microscopy at 100$\times$ magnification (see Supplementary Material). The initial concentrations varied depending on differences in the solubilities and vapor pressures of the materials. Aliquots of 20μL of HEMs standard solutions were deposited on one side of the SS substrates and then evenly distributed using a sample smearing method[26]. Isopropanol was used as the solvent for RDX, TNT, and 2,4-DNT, while dichloromethane was used for TATP because of its high vapor pressure, which means that a more volatile solvent is required. For the determination of thermodynamic properties, MIR spectra were recorded as a function of time at different temperatures. For TATP, initial surface loadings (Cs$_\circ$) of 25, 50, and 80 μg/cm^2 were used within the range of temperatures 14-36 °C. The Cs$_\circ$ values for 2,4-DNT and TNT were 2.8, 5.7, and 11.4 μg/cm^2; and 3.8, 7.6, and 11.4 μg/cm^2, respectively. The temperatures studied were 23-60 °C for 2,4-DNT and 22, 30, 40, 50, 55 and 70°C for TNT. For RDX, only Cs$_\circ$ values of 0.7 and 1.4 μg/cm^2 were studied at 22, 44, 65, 75,

and 80°C. For each temperature, the measurements were carried out in triplicate. The sublimation rate of RDX at room temperature (22 °C) was monitored over 258 days to consider the signal decay.

2.6. Desorption energy

Due to the low vapor pressure of RDX, its desorption energy was also studied by TDS. A temperature-programmed method (TPM) was used. A first-order desorption rate (r_{des}) was obtained for the RDX on SS substrates. For a first-order rate, the value of surface concentration or surface loading (Cs) is proportional to the r_{des} and corresponds to the simplest case of single molecules desorbing directly and independently from sites on the surface. The r_{des} is related to Cs and T via Eq.5. The units for k and k° are s^{-1} (frequency units) and these are related to each other and to $\Delta_{des}U$, k°, and the Boltzmann constant (k_B) through an Arrhenius type relationship (Eq.5). This frequency is called the attempt frequency, and it is of the order of crystal lattice atomic frequencies ($\cong 10^{13}$ s^{-1})[34].

$$r_{des} = -\frac{dCs}{dt} = kCs^n = k°Cs^n exp\left(-\frac{\Delta_{des}U}{k_B T}\right) \tag{5}$$

where n is the surface desorption rate order. It is assumed that all adsorbed molecules occupy identical sites on the surface and that they do not interact with each other. In TPM, there are two possible regimes of data acquisition: flash desorption and adiabatic (slow) desorption. Slow desorption is commonly used for TPM by TDS. Here the vapor pressure (p) is proportional to r_{des}, and the heating rate (β_h = dT/dt) used must be linear. Then, Eq.5 is transformed into Eq.6:

$$p(T) \propto -\frac{dCs}{dt}\frac{1}{\beta_h} = -\frac{dCs}{dT} = \frac{k°Cs^n}{\beta_h}exp\left(-\frac{\Delta_{des}U}{k_B T}\right) \tag{6}$$

The desorption rate divided by the heating rate (r_{des}/β_h) increases at the beginning of the temperature ramp on sample heating but decreases at the end of the temperature program because the adsorbate coverage is spent. The vapor pressure depends on T and has a maximum value at Tmax that is related to $\Delta_{des}U$, to the desorption rate order (n), and k°. In the case of first-order kinetics,[35] Eq.6 is derived and set equal to zero to find the maximum:

$$ln\left(\frac{\beta_h}{T_{max}^2}\right) = -\frac{\Delta_{des}U}{k_B}\frac{1}{T_{max}} + ln\left(\frac{k°k_B}{\Delta_{des}U}\right) \tag{7}$$

To measure Cs with time and temperature, GAO measurements using polarised MIR light were used. IR reflectance spectra were measured at different $\beta_{sub}h$ and initial surface loadings (Cs$_\circ$). The relationship between Cs, density (ρ), and thickness (d) is shown in Eq.8, and the relationship between $\Delta R/R_\circ$ (where R is the reflectance, ΔR is R$_\circ$-R, and R$\circ$ is the baseline reflectance) and d is given inEq.8[36]:

$$d = \frac{Cs}{\rho} \tag{8}$$

$$\left(\frac{\Delta R}{R_\circ}\right)_s \cong 1 - R_s \cong -8\pi d\nu Im(\epsilon)cos(\phi) \propto Cs \tag{9}$$

or

$$\left(\frac{\Delta R}{R_\circ}\right)_p \cong 1 - R_p \cong -8\pi d\nu Im\left(\frac{1}{\epsilon}\right)sin(\phi)tan(\phi) \propto Cs \tag{10}$$

where R$_s$ is the reflectance with the component of the electric field vector E$_s$ oriented perpendicular to the plane of incidence, R$_p$ is the component of the electric field vector E$_p$ oriented parallel to the plane of incidence, ν is the frequency of vibration of some mode, ϕ is the angle of incidence, Im(ϵ) is the imaginary part of the dielectric constant of the substance deposited (or energy loss function),

166 and $Im(1/\epsilon)$ is the imaginary part of the inverse dielectric constant of the substance deposited (or
167 longitudinal optical energy loss function). Combing Eq.8, Eq.9 and Eq.10, a relationship between
168 $(\Delta R/R_\circ)_{s,p}$ and Cs is derived. Eq.9 and Eq.10 can be well approximated for d « λ where λ is the
169 IR wavelength, which is in the order of 10,000 nm or larger. Values of d between 1 to 100 nm are
170 considered ideal values.
171   Logistic sigmoid fits were obtained from plots of $\Delta R/R_\circ$ vs. T for various modes and substances
172 (see Eq.11), where A, B, and $a_\circ$ are constants. Next, the derivative of $\Delta R/R_\circ$ with respect to T was

$$\left(\frac{\Delta R}{R_\circ}\right) = \left(\frac{\Delta R}{R_\circ}\right)_s + \left(\frac{\Delta R}{R_\circ}\right)_p = \frac{A}{1 + exp\left(a_\circ\left(T - T_{max}\right)\right)} + B \tag{11}$$

3. Results and discussion

3.1. Spectroscopic signatures

175   Fig.2a to 2d show the decay of the vibrational IR signals for the HEMs studied. IR spectra were
176 recorded every 12 s using GAP spectroscopy. For TATP, the peak area (A_p) between 1330 and 1407
177 cm^{-1} was calculated for each spectrum. Two bands located in the wavenumber range 1330-1407 cm^{-1}
178 were selected because they are isolated and are relatively narrow in comparison with the others. These
179 vibrations were assigned as the out-of-plane bending of the methyl group $\delta_{as}(CH_3)$ by Buttigieg et
180 al.[37] Brauer et al.[38] assigned that combination to CCC asymmetric stretching and CCO bending.
181 For 2,4-DNT and TNT, the prominent signal located at 1343 cm^{-1} was used. This signal was assigned to
182 C-NO$_2$ vibration coupled to C-N stretching[39–41] (Fig.2b and 2c). This band was used for monitoring
183 the kinetic behavior of the nitroaromatic compounds. The range used to calculate the areas was
184 1324-1372 cm^{-1}. A_p for a characteristic MIR region has an exponential decay. Thus, a fit to a natural
185 logarithm function in terms of ln ($A-A_\infty$) vs. time was applied to determine the sublimation constants
186 (k) for TATP, 2,4-DNT, and TNT from the slopes (see Supplementary Material). Fig.2d shows the decay
187 of the IR signals for RDX. The behavior of the area for the band at 1264 cm^{-1} and the band at 1321 cm^{-1}
188 (N-NO$_2$ symmetrical stretching[42–47]) vs. time are approximately linear. However, the IR intensity
189 decay vs. time is exponential for the 1593 cm^{-1} band (N-NO$_2$ asymmetrical stretching[42–44]). To
190 determine the true behavior of RDX sublimation, a calibration curve using multivariate chemometrics
191 methods was obtained and used for the prediction of Cs. Next, Cs vs. time was plotted, and the
192 exponential behavior was observed.

3.2. Determination of surface concentration and thickness for RDX

194   Calibration curves were prepared with the GAP spectral data for RDX using a PLS regression
195 algorithm[48–52] in the Quant2 software package by Bruker Optics OPUS (version 4.2). Samples
196 with RDX surface loadings were prepared using a smearing method[26,53–55] at room temperature.
197 Thirty-six standard Cs from 100 to 1000 ng/cm^2 were used for the calibration curve. The Cs standards
198 were verified using a high-performance liquid chromatography (HPLC) technique reported by
199 Wrable-Rose et al.[56] (See Supplementary Material). The regions used for the analyses were 1000-1260
200 cm^{-1}, 1314-1380 cm^{-1}, and 1560-1634 cm^{-1}. Vector normalization (VN) pre-processing was applied
201 to the spectroscopic data. VN normalizes a spectrum by first calculating the average intensity value
202 and subsequent subtraction of this value from the spectrum. Then, the sum of the squared intensities
203 is calculated, and the spectrum is divided by the square root of this sum. This method is used to
204 account for differences in samples thickness[57]. Cross validations were performed, and the root mean
205 square errors of cross validations (RMSECVs), root mean square errors of estimations (RMSEEs), and
206 correlation coefficient squared (R^2) were used as criteria to evaluate the quality of the correlations
207 obtained. The optimum calibration curve had an RMSEE of 6 ng/cm^2, an RMSECV of 8 ng/cm^2, an
208 R^2 of calibration of 0.9997, and an R^2 of validation of 0.9993. The model was obtained from 5 loading
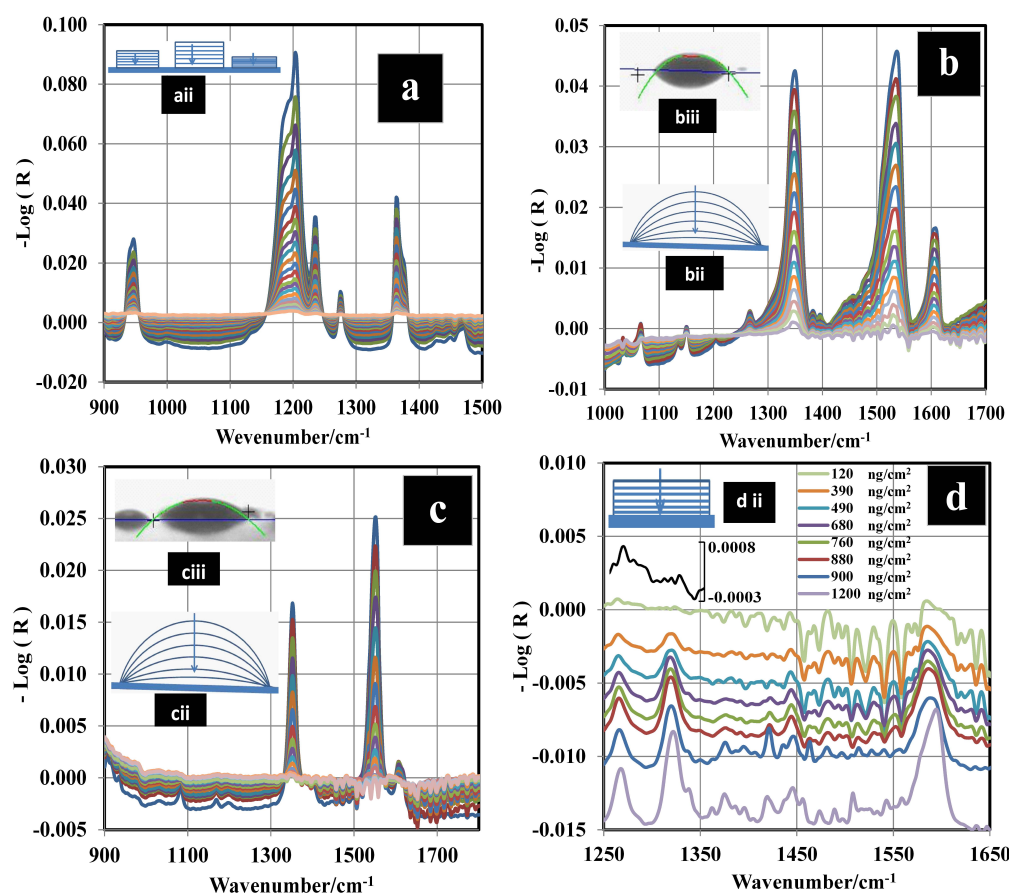
Figure 2. MIR reflectance spectra for different HEMs undergoing sublimation on SS surfaces. (a) TATP at 24 °C, (b) 2,4-DNT at 35 °C, (c) TNT at 70 °C and (d) RDX at 80 °C.

vectors for the spectroscopic data, and the significance of the statistics was at the level of p = 0.0001. The limit of detection (LOD) was calculated according to Eq. 12[58–60] where $\Delta(\alpha,\beta,g)$ is a statistical parameter that takes into account the α_p and β_p probabilities of falsely stating for the g free degree, and the leverage, $h_\circ$, quantifies the distance of the predicted sample at zero concentration level to the mean of the calibration set. Fig.3 shows the PLS model derived from the data and the ideal model (y = x).

$$LOD = \Delta(\alpha_p, \beta_p, g))RMSEE(1 + h_\circ)^{0.5} \qquad (12)$$

The value obtained for the LOD with the PLS model was 22 ng/cm^2. A second model using classical least squares (CLS) regression (or linear regression) was used for comparison. The results are shown in Fig.3 where the peak areas at 1321 cm^{-1} were used for the regression. Peak areas are shown on a second y-axis in Fig.3. The correlation coefficient obtained was R^2 = 0.9896, and the LOD value was 103 ng/cm^2 . This was calculated as three times the standard deviation of the intercept between slopes[61,62]. The LOD for this model is larger than the one obtained using PLS because the signal at 1321 cm^{-1} disappears almost entirely for a surface loading of 120 ng/cm^2 (Fig.2d). This does not happen for the signal at 1594 cm^{-1}, but a good linear CLS model could not be obtained for this signal. As shown in Fig.4, the predicted Cs from the PLS model vs. time exhibits exponential behavior. The value of k was determined for various temperatures (see Supplementary Material). When the surface concentration is low, several bands disappear. However, the vibrational signals in the range 1400-1650 cm^{-1} are highly persistent. A red shift is observed when the concentration diminishes or approaches monolayer coverage. In particular, red shifts of 2 cm^{-1} for the band at 1321 cm^{-1} and 3 cm^{-1} for the

band at 1268 cm^{-1} are observed (see Fig.2d). A larger red shift for the band at 1594 cm^{-1} is observed (6 cm^{-1}), but it is not possible to determine it exactly because vibrational signals for water are present in this range.
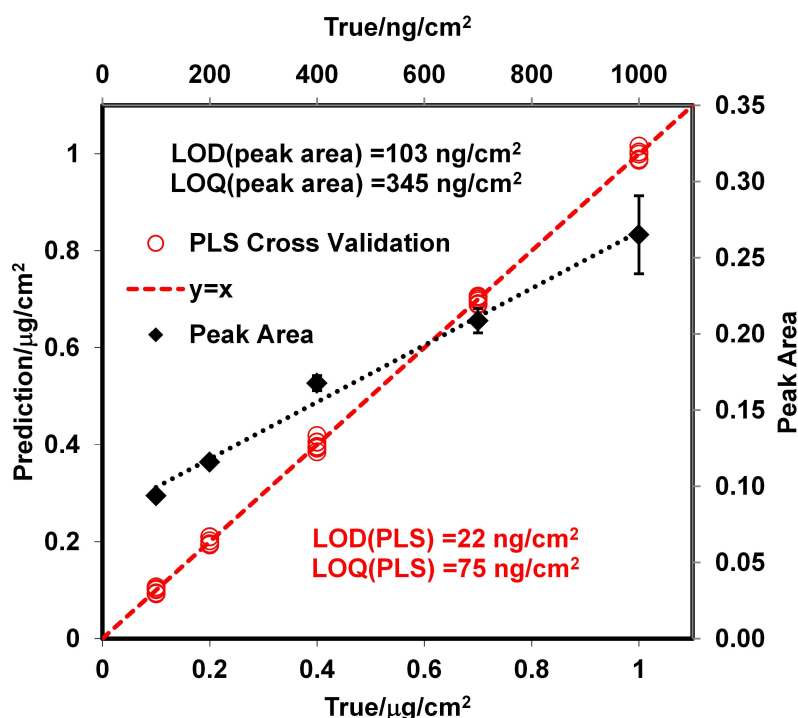

Figure 3. Calibration curves for RDX on SS by CLS and PLS models.

At low surface concentrations where RDX is near to monolayer coverage, the effect of the interaction of RDX with the surface is most noticeable. RDX can interact with the metal surface through the NO$_2$ group. This weakens the NO bond, thus explaining the red shift as well as the smaller red shift exhibited by the N-NO$_2$ symmetric stretching band. The NO$_2$ group interacts with the surface, reducing its mobility. This adds another component to the reduced mass of the oscillator, causing a decrease in frequency. Only one peak at 1594 cm^{-1} is observed for this layer, but two bands are typically exhibited by bulk samples at room temperature (α phase polymorph of RDX). The peaks in the spectrum of bulk RDX are observed at 1574 and 1596 cm^{-1} (see Supplementary Material). It has been suggested that the β phase crystalline polymorph of RDX (β-RDX)[42] is present in this layer (see Fig.2d and Supplementary Material). α-RDX and β-RDX are conformational polymorphs[63] that can be differentiated using vibrational spectroscopy (Raman or MIR).

3.3. GAP vs. GAO measurements for RDX

A validation of GAP for RDX was carried out by comparing the results from GAP measurements with those obtained using GAO. No significant spectral differences between GAP and GAO spectra were observed for the range 1000-1600 cm^{-1} (see Supplementary Material). However, a difference in the instrument detection capability was observed. The calculated signal-to-noise ratios (SNRs) for measurements using GAP were much larger than the corresponding values obtained by calculations using GAO measurements, particularly when the number of scans is small. These differences in SNRs decrease when the number of scans is large. Table 1 shows the SNRs for GAP and GAO for different numbers of scans. The signal at 1594 cm^{-1} was used to calculate the values of the SNRs, and the noise was calculated from root mean square (RMS) values for baseline levels in the 1900-2100 cm^{-1} region. GAP measurements show a higher SNR at a low number of scans because the area averaged is larger than that for GAO and spatial averaging of a large area tends to decrease the noise levels
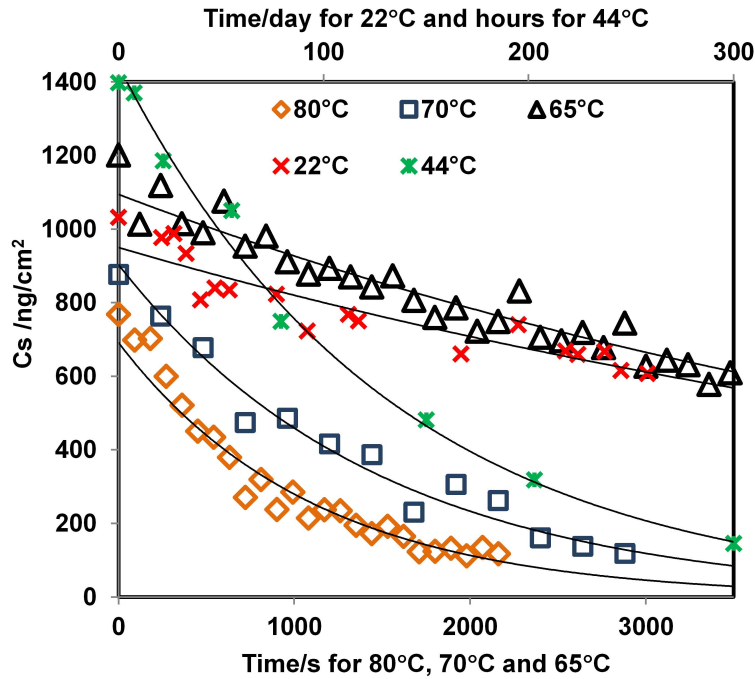
Figure 4. Prediction of Cs using the PLS model vs. time for RDX on SS at different temperatures.

obtained. This suggests that GAP may be used for measuring surface kinetic processes that require small time intervals (the time for one scan at a resolution of 4 cm^{-1} and 10 KHz scanning velocity is approximately 0.5 s).

Table 1. Comparison of signal-to-noise ratios for GAP and GAO measurements.

	GAP		**GAO**	
Scan	Noise	SNR	Noise	SNR
1	0.00069	24	0.00160	4
5	0.00025	28	0.00130	5
10	0.00020	35	0.00120	7
20	0.00019	36	0.00035	20
50	0.00019	37	0.00035	23
120	0.00019	38	0.00030	23

3.4. Sublimation enthalpies and desorption energies

Two different methods were used to determine $\Delta_{sub}H$, i.e., TGA and GAP, and a third was used to determine the desorption energy, i.e., TPM ($\Delta_{des}U$). Using the TGA approach, $\Delta_{sub}H$ was calculated from a linear fit of -R$_g$ln(v_s) and 1/T, where the slope corresponds to the enthalpy of sublimation and R$_g$ is the ideal gas constant. This approach worked well for all cases except for TATP, because in this case, the fit was not linear (see Fig. 5). For TATP, a multiple regression analysis was performed in which -R$_g$ln(v_s) was related to a three-term fit; 1/T, ln(1/T), and a constant (see Eq.13)[64]. Next, the derivatives with respect to 1/T for the simple linear models and for the multiple-terms model were obtained to calculate the $\Delta_{sub}H$ for the bulk phase of the HEMs studied (see Eq.14 and Eq.15).

$$ -R_g ln\left(\zeta\right) = a\frac{1}{T} + bln\left(\frac{1}{T}\right) + c \qquad (13) $$

$$\Delta H = -R_g \left(\frac{\partial ln(\nu_s)}{\partial \left(\frac{1}{T} \right)} \right) = -R_g \left(\frac{\partial ln(k)}{\partial \left(\frac{1}{T} \right)} + T \right) = \Delta_{sub} U + R_g T \tag{14}$$

where ζ is k or ν_s. The model described by Eq.13 was evaluated using the p-value of the model and the parameters a, b, and c, and the correlation coefficient (R^2). A value of p < 0.0001 was found for the parameter and models, indicating a high statistical significance for both TGA and GAP for TATP. The model in Eq.13 was used for TATP, but when this was applied for the other explosives, the p values indicated insufficient significance. This indicates a simple linear behavior of ln(ν_s) vs. 1/T, and that the changes in heat capacity (ΔC_p) are near zero (or that their values are within the errors of the experiment). This result indicates that the change in the heat capacity is more significant in the temperature range studied for TATP than for the other explosives.

$$\Delta H(T) = a + bT = \Delta H_{mean} + \Delta C_p \left(T_{mean} - T \right) \tag{15}$$

The GAP and TGA data for TATP were evaluated using a non-random residual analysis for simple linear models, and a random residual for the model described with Eq.13. For the other explosives, a random residual trend for the simple linear models was observed. The advantages of the model described by Eq.13 is that the first derivate with respected to 1/T is a linear function of T. ΔH can be calculated for every temperature in the range evaluated from Eq.15, where ΔC_p is the difference between the heat capacity of TATP in the gas phase and that in the solid phase ($\Delta C_p = C_p$(solid) - C_p(gas) = -b), The uncertainties in ΔH in the media temperature should be lower than for every other temperature[65]. Uncertainties (σ) in ΔH were calculated from Eq.17, where σ_{yD} is a direct contribution from the model and σ_{yI} is an indirect contribution[66] calculated from the propagation of uncertainties[67] (see Supplementary Material).

$$\sigma_y^2 = \sigma_{yD}^2 + \sigma_{yI}^2 \tag{16}$$

$$\sigma_{\Delta H}^2 = \left(\delta_T b \right) + \left(\left(T - T_{mean} \right) S_b \right)^2 + \left(\frac{s_r \Delta H}{-R_g Ln(\zeta)} \right)^2 \tag{17}$$

$$\sigma_{\Delta H_{mean}}^2 = \left(\delta_T b \right) + \left(\frac{s_r \Delta H_{mean}}{-R_g Ln(\zeta_{mean})} \right)^2 \tag{18}$$

In the current study, δ_T is of the order of 0.001 K/T for TGA and 0.1 K/T for GAP, S_b is the standard deviation of b, σ_{yD} is ΔH_{mean} plus the standard error of the model in Eq.13 divided by $-R_g ln(\zeta)$, where ζ is k or ν_s (see Eq.17). σ at media temperatures ($\sigma_{\Delta H}$) can be obtained using Eq.18.

TPM was used to obtain the energy of interaction between the HEM and the surface. There are three possible hypotheses for a substance deposited on a surface. First, if the energy of interaction ($\Delta_{int}U$) has a value comparable to $\Delta_{sub}H$ or lower, then the value of $\Delta_{des}U$ can be approximated by the sum of $\Delta_{int}U$ and ($\Delta_{sub}H$ - $R_g T_{mean}$). Second, if $\Delta_{int}U$ is zero or very small, then $\Delta_{des}U$ is approximately $\Delta_{sub}H$ - $R_g T_{mean}$. Third, if $\Delta_{int}U$ is larger than $\Delta_{sub}H$, two decays of Cs should be observed by TPM; first, a decay of bulk coverage by sublimation followed by a second decay of the monolayer coverage. The values for the calculated thermodynamic parameters $\Delta_{sub}H$ and $\Delta_{des}U$ $\Delta_{sub}H$ were calculate from $\Delta_{des}U + R_g T$ are shown in table 2. Three models were obtained for TATP from TGA measurements. The first model for the sublimation obtained from the rate of sublimation measurements at different temperatures used a ΔT of 5 ° C (see Fig.5; label as TATP_TGA_1; table included as part of the Supplementary Materials). The rates were measured at 1 °C and 0.5 °C (see Fig.5). Labels used were TATP_TGA_2 and TATP_TGA_3, respectively. The table containing these results can also be found in the Supplementary Materials. The TGA experiments for TATP were performed in triplicate to prove that it was not a simple linear case. The samples used came from two different syntheses, and the
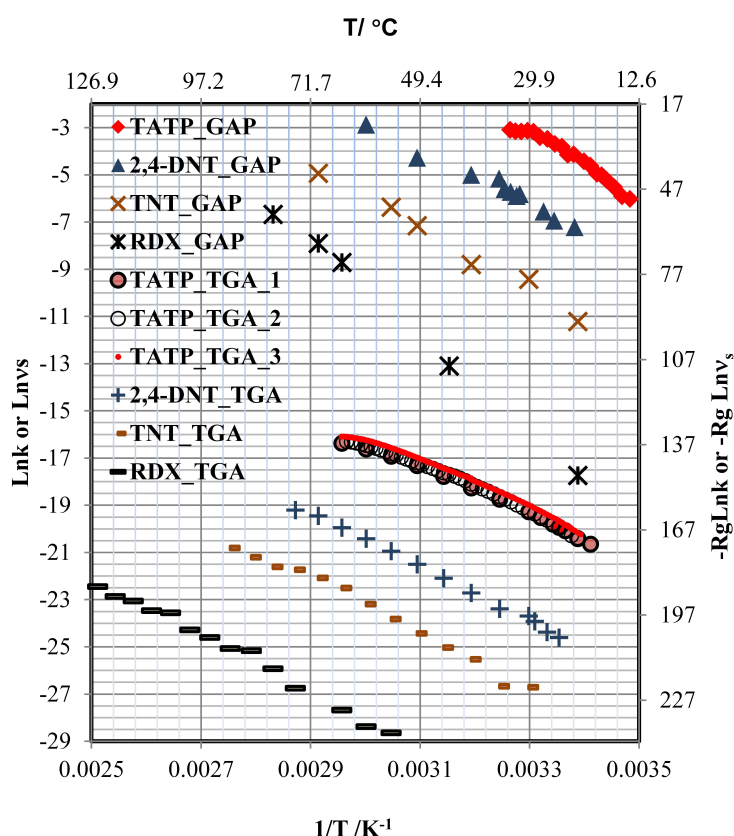
Figure 5. Arrhenius plots of GAP and TGA data used to obtain the sublimation rates for TATP, 2,4-DNT, TNT, and RDX. The units for GAP are s^{-1} and for TGA are kg*s^{-1}.

301   time difference between the two sets of experiments was six months. $\Delta_{sub}H$ at T_{mean} = 37.82 °C was
302   83 ± 5 kJ/mol for the first experiment and 87 ± 3 kJ/mol and 86 ± 2 kJ/mol at T_{mean}= 43.00 °C and
303   T_{mean} = 37.80°C, respectively, for the second and third experiments. The value of $\Delta_{sub}H$ for TATP
304   using GAP was 140 ± 14 kJ/mol at T_{mean} = 20.9 °C. These values are different to that obtained by
305   TGA, but the $\Delta_{sub}H$ values obtained by TGA in the temperature range 24-27 °C (calculated by Eq.15)
306   are statistically identical to $\Delta_{sub}H$ obtained by GAP (see Table 3 and Supplementary Materials). This
307   suggests that the interaction between TATP and the substrate is very weak and that sublimation is the
308   main phenomenon involved.

Table 2. Enthalpy of sublimation for HEM and desorption energy for RDX on SS.

Exp	HEM	Range of T	T_{mean} / °C	$\Delta_{sub}H$	R^2
GAP	TATP	14−33	20.9	144 ± 14	0.997
TGA_1	TATP	20−65	37.5	83 ± 5	0.999
TGA_2	TATP	22−64	44.0	87 ± 3	1.000
TGA_3	TATP	21−63	37.8	86 ± 2	1.000
GAP	2,4-DNT	23−35	36.0	94 ± 5	0.986
TGA	2,4-DNT	25−75	46.6	94 ± 2	0.998
GAP	TNT	40−70	55.0	111 ± 6	0.998
TGA	TNT	40−65	52.5	95 ± 3	0.997
GAP	RDX	22−80	56.2	153 ± 5	0.998
TGA	RDX	55−125	90.0	99 ± 3	0.987
TPM	RDX	ΔU/kJ/mol	β_h /°C/min	T_{max}/°C	
		$\Delta_{int}U$ =19±1	5	117 ± 2	
			10	142 ± 3	
			20	200 ± 3	

The values obtained for ΔC_p by TGA and GAP are different. For TGA, the values are 1.21 ± 0.09 kJ/mol*K, 1.50 ± 0.04 kJ/mol*K and 1.24 ± 0.04 kJ/mol*K, while that with GAP is 8.6 ± 0.9 kJ/mol*K. It is possible that in GAP, the SS surface can affect the measured values due to the heat transferred from the surface and the surroundings. This hypothesis is confirmed by the fact that at room temperature, the $\Delta_{sub}H$ values obtained by TGA and GAP are statistically identical, where heat transfer from the surface to the surroundings is almost zero. For TGA experiments, the temperature of the surroundings is equal to the sample temperature for all isothermal measurements, but for GAP, this only occurs at room temperature. This difference in $\Delta_{sub}H$ in the absence of $\Delta_{int}U$ is only observed for explosives where ΔC_p is statistically different from zero. This is confirmed by fitting the model of Eq.13 to 2,4-DNT, TNT, and RDX for the ΔC_p values obtained by GAP and TGA.(see Table 3). There are no significant differences statistically between the values obtained by GAP and TGA because the values of ΔC_p for these explosives is in the order of the experimental uncertainties, although for RDX in GAP the crystalline phase is β (β-RDX) and in TGA is α (α-RDX).

Table 3. Enthalpies of sublimation for standards (kJ/mol) and ΔC_p (kJ/mol*K) for HEMs.

Molecule	$\Delta_{sub}H°$ for GAP	$\Delta_{sub}H°$ for TGA	$\Delta_{sub}H°$ for TGA_2	$\Delta_{sub}H°$ for TGA_3
TATP	104 ± 15	99 ± 6	107 ± 3	102 ± 3
2,4-DNT	103 ± 11	100 ± 5		
TNT	117 ± 31	120 ± 9		
RDX	165 ± 22 for β-RDX	112 ± 20 for α-RDX		

Molecule	ΔC_p for GAP	ΔC_p for TGA	ΔC_p for TGA_2	ΔC_p for TGA_3
TATP	8.6 ± 0.9	1.21 ± 0.09	1.50 ± 0.04	1.24 ± 0.04
2,4-DNT	1.1 ± 0.9	0.3 ± 0.2		
TNT	0.3 ± 1.0	0.9 ± 0.3		
RDX	0.4 ± 0.7	0.2 ± 0.3		

The non-linear behavior of TATP and the high value of ΔC_p can be explained by the difference in the values of $\Delta_{sub}H$ found in the literature (see Table 4). For the value of ΔC_p obtained from Eq.13, it was necessary for both methodologies to obtain many points of temperature and use a large range of temperatures. Data from the literature was used to obtain ΔC_p (see Table 4). For experiments at relatively low temperatures, ΔC_p is near to zero, and the fit is linear. This can also be observed in Fig. 5. The curvature is only prominent at high temperatures. The values of ΔC_p from Oxley et al. are comparable to the present results. This can be attributed to the fact that they used a small number of temperature values, which is required to obtain low uncertainties in ΔC_p.

Table 4. Enthalpies of sublimation and ΔC_p values for TATP from this study and the literature.

	T_{mean} in $°C$	N of T	ΔC_p in kJ/mol*K	$\Delta_{sub}H$ in kJ/mol
GAP	20.9	19	8.6 ± 0.9	142 ± 14
TGA_1	37.5	14	1.21 ± 0.09	83 ± 5
TGA_2	44	42	1.50 ± 0.04	87 ± 2
TGA_3	37.8	88	1.24 ± 0.03	85 ± 2
Damour et al 2010[67]	14.3	27	0	86.2 ± 1
Ramirez et al 2006[22]	50.0	7	0.75 ± 0.08	85.8
Felix et al. 2011[68]	50.0	8	-	72.1
Oxley et al. 2005[69]	40	6	0.3 ± 0.5	109
Oxley et al. 2009[70]	32.2	7	0.6 ± 0.7	73
Dunayevskiy et al. 2007[71]	0	-	-	81.3
Espinosa-Fuentes et al. 2015[72]	46	32	1.5	103.8 ± 0.2

For 2,4-DNT and TNT, the materials deposited for GAP experiments do not exist in solid crystalline forms. Rather, they adopt metastable phases in the form of droplets (see Supplementary Material). The contact angle (CA) for the droplets are $42 \pm 3°$ for 2,4-DNT and $35 \pm 1°$ for TNT (see Figs.2biii and 2ciii), indicating that 2,4-DNT has slightly less affinity for the surface than TNT. The CA changes during the sublimation process. This can be explained from the microscopic viewpoint in that molecules that interact directly with the surface and neighbors cannot be desorbed to the gas phase as easily as molecules that are far away from the surface and that are able to pass directly to the gas phase, generating a change in CA without a change in the enthalpy of sublimation. This behavior is illustrated in Figs.2bii and 2cii). The mechanism is similar for 2,4-DNT and TNT. This is corroborated by the existence of an isokinetic temperature found for the plot Ln(k) vs. 1/T. The value found for the plot was 666 K. The estimated $\Delta_{sub}H$ for the metastable forms are 91 ± 5 and 108 ± 6 kJ/mol for 2,4-DNT and TNT, respectively, assuming that the interactions between the HEM and the surface are negligible. A contribution from $\Delta_{int}U$ for 2,4-DNT and TNT cannot be ruled out because the end of the sublimation of the droplets leaves a film of molecules that were interacting with the surface initially. However, the value of $\Delta_{int}U$ for this film should be too small to be measured by TPM with TDS using GAO. The TGA method for TNT and 2,4-DNT revealed $\Delta_{sub}H$ values for the crystalline phases of 95 ± 3 and 94 ± 3 kJ/mol, respectively. These values are close to the literature values (see Table 5). $\Delta_{sub}H$ for the crystalline phase is statistically similar to $\Delta_{sub}H$ for the metastable phase for TNT and DNT. The metastable form is described as a supercooled liquid[14]. It is possible to induce the transition from the metastable phase to crystalline phase by applying mechanical pressure. This process destabilizes the pseudo equilibrium of the metastable form and induces a change in state to the more stable crystalline form.

The size of the droplets depends on the Cs as generated in the smearing deposition method. A size distribution was obtained for different Cs values. A normal distribution was observed for TNT at all concentrations when alcohols are used as solvents in the deposition process. The distributions for 2,4-DNT are far from normal at low Cs. The distributions were obtained by capturing several images for a selected Cs and measuring the size of the droplets from the image obtained (see Supplementary Material). This analysis is important for the development of standards for solids deposited on substrates for use in explosives-detection devices. This explains the higher RMSECV for 2,4-DNT than for TNT found by Primera et al.[53,54] When RDX was deposited on the metal surface from isopropanol solutions, films were observed (see Figs.2diii and Supplementary Material). These films are made of β-RDX polymorph, different from the bulk solid. In bulk solid, α-RDX polymorph is observed. Several previous studies have reported that the β-RDX conformer is metastable[63] relative to the α-RDX conformer. The energy difference between the two conformations is less than 1 kcal/mol[43,73–75]. The β-RDX polymorph was also formed when the RDX sample was allowed to sublimate and condense on a glass slide and upon depositing the sample from solutions[44] of various solvents (acetone, methanol, or saturated isopropanol). This is supported by the MIR spectrum and
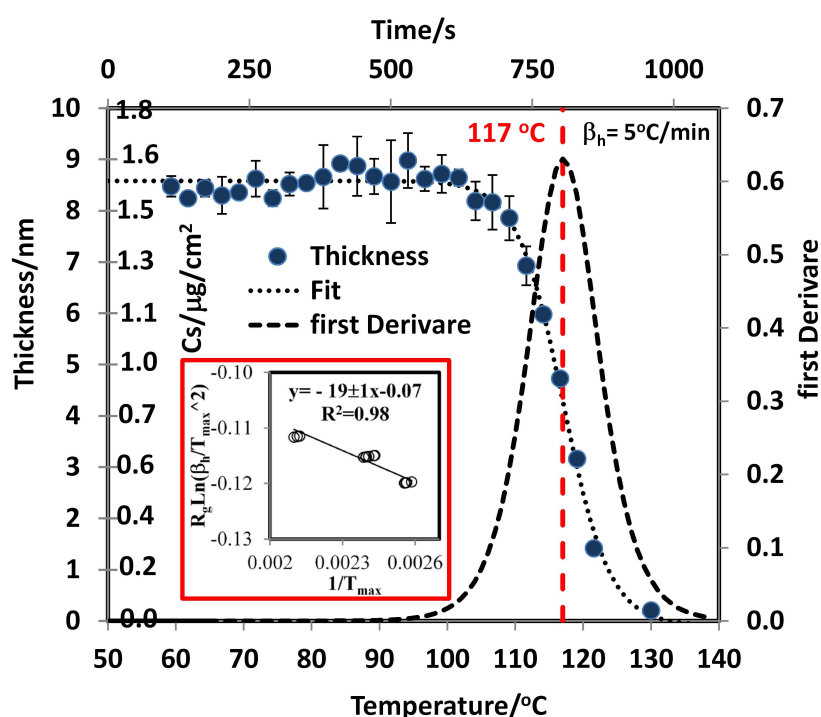
Figure 6. Plot of thickness vs. T(°C) from TPM-TDS and d(ΔR/R)/dT vs. T.

discussed above. Sublimation of solid α-RDX and a β-RDX film were measured by TGA and GAP, respectively, and $\Delta_{sub}H$ for the α-RDX and β-RDX phases were obtained. The calculated value for α-RDX is 99 $\pm$ 3 kJ/mol (Table 2). The value obtained by the GAP method for RDX is 169 $\pm$ 5 kJ/mol. This value is $\Delta_{sub}U + \Delta_{int}U$. TPM was used to obtain $\Delta_{int}U$. Measurement of R for five bands (1576 cm^{-1}, 1534 cm^{-1}, 1316 cm^{-1}, 1268 cm^{-1}, and 909 cm^{-1}) in the spectrum of RDX at three different β_h values were used to obtain T_{max} from the first derivate of a logistic fit (Eq. 11; Fig.6 and red square inset in Fig.6). Next, $-R_g \ln(\beta_h/T_{max}^2)$ vs. $1/T_{max}$ was plotted to determine the value of $\Delta_{int}U$ from the slope of the fit (Eq. 7). $\Delta_{int}U$ was found to be 19 $\pm$ 1 kJ/mol, and $\Delta_{sub}U$ for β-RDX now becomes 150 $\pm$ 5 kJ/mol and $\Delta_{sub}H$ becomes 153 $\pm$ 5 kJ/mol. This value is larger than the corresponding value for α-RDX.

Table 5. Enthalpies of sublimation for DNT, TNT, and RDX in this study and the in literature.

HEM	Autor	$T_{mean}/°C$	$\Delta_{sub}H$
DNT	This work from GAP	36	94 ± 5
DNT	This work from TGA	46.6	94 ± 2
DNT	Lenchitz 1970[76]	64	98.3 ± 2.5
DNT	Lenchitz 1970[76]	25	99.6 ± 2.5
DNT	Felix et al. 2011[68]	52.4	96.2
DNT	Pella 1976[77]	37	95.80 ± 1.25
DNT	Lenchitz 1971[78]	–	99.6 ± 1.3
TNT	This work from GAP	55	111 ± 6
TNT	This work from TGA	52.5	95 ± 3
TNT	Edwards 1950[79]	–	118.4
TNT	Dionne et al. 1986[80]	25	113
TNT	Gershanik et al. 2010[81]	40	97 ± 7
TNT	Oxley et al. 2005[69]	36	137
TNT	Eiceman et al. 1997[82]	114.5	87
TNT	Leggett 1977[83]	26	141.1 ± 0.2
TNT	Hikal et al. 2014[84]	67.5	95.9 ± 1
TNT	Hikal et al. 2011[85]	–	100.2
TNT	Mu et al. 2003[86]	32.5	131
TNT	Chickos et al. 2002[87]	35	112.4
TNT	Cundall et al. 1978[88]	25	113.2 ± 1.5
TNT	Felix et al. 2011[68]	54.8	106.8
TNT	Pella 1977[89]	–	99.2 ± 2.0
TNT	Lenchitz 1971[78]	25	104.6 ± 1.7
TNT	Lenchitz 1970[76]	65	103.3 ± 2.5
TNT	Jones 1960[90]	–	118.4 ± 4.2
TNT	Hikal 2019[91]	55	105.9 ± 1.4
TNT	Hikal 2019[91]	55	102.1 ± 2.7
TNT	Hikal 2019[91]	55	105.8 ± 1.6
TNT	Lee 2019[92]	18.5	104.4 ± 2.4
RDX	This work from GAP	56.2	150 ± 5
RDX	This work from TGA	90	99 ± 3
RDX	Rosen et al. 1969[93]	–	130.2
RDX	Gershanik et al. 2012[94]	65	115 - 134
RDX	Eiceman et al. 1997[82]	130	115
RDX	Hikal et al. 2011[85]	–	128
RDX	Hikal et al. 2014[84]	120	130 ± 2
RDX	Cundall et al. 1978[88]	25	134.3
RDX	Felix et al. 2011[68]	92	99.5
RDX	Chickos et al. 2002[87]	–	112.5 ± 0.8
RDX	Rosen et al. 1969[93]	77	130.1

4. Conclusions

Sublimation enthalpies were measured using GAP for materials that do not interact strongly with the surface and where ΔC_p in the temperature range of the study is zero or negligible. This is not the case for TATP because of a high value of ΔC_p was observed. The unexpected, temperature-dependent value for ΔC_p for TATP may be related to its high sensitivity to heat, friction, and shock. Using GAP, it was possible to differentiate between different phases and conformations of the materials. Using MIR techniques, the residence time of materials on surfaces was monitored, and the rates of sublimation of the materials from the surfaces were measured. The superiority of GAP over GAO found is based on the detection sensitivity due to the high coverage area used in GAP. Using GAP, it is possible to detect highly energetic materials on metallic surfaces at the macro scale in 0.5 s (1 scan). Different types of mechanisms for sublimation on surfaces were found for the HEMs studied. For TATP, the sublimation takes place from small crystals to groups of islets. For 2,4-DNT and TNT, sublimation occurs from droplets that are part of a metastable phase. RDX is sublimated from a seemingly uniform coverage

layer formed on the surface. The type of crystal phase that the HEMs assume on the substrate depends on surface-adsorbate adhesion forces vs. adsorbate-adsorbate intermolecular forces. Interactions between the HEMs and the surface can influence the rate of sublimation from the surface. The presence of this substrate-adsorbate interaction is demonstrated by the shift in the vibrational signals of RDX upon interaction with the SS substrate. For the case in which the interaction forces between the explosive and the surface are weak, the desorption energy should be minor compared to the sublimation enthalpy measured by TPM.

Author Contributions: conceptualization, L.P., M.R., and R.I.; methodology, L.P., M.R., and R.I.; validation, L.P., N.G. and S.H.; formal analysis, N.G., J.R., and L.P.; investigation, L. P., M.R., N.G., J.R.,and R.I.; resources, S.H.; writing–original draft preparation, L. P., M.R., N.G., J.R., R. I. and S.H.; writing–review and editing, L. P. and S.H.; visualization, L.P., N.G., and J.R.; project administration, L.P. and S.H.; funding acquisition, S.H.

Abbreviations

The following abbreviations are used in this manuscript:

GAP	grazing angle probe fibre optic
GAO	grazing-angle objective
HEM	highly energetic material
TGA	thermogravimetric analysis
TDS	thermal desorption spectroscopy
TPM	temperature-programmed method
TATP	triacetone triperoxide
DNT	2,4-dinitrotoluene
TNT	2,4,6-trinitrotoluene
SS	stainless steel
$\Delta_{des}U$	desorption energy
$\Delta_{sub}H$	enthalpy of sublimation
MCT	mercury cadmium telluride

References

1. Mamo, S.K.; Gonzalez-Rodriguez, J. Development of a Molecularly Imprinted Polymer-Based Sensor for the Electrochemical Determination of Triacetone Triperoxide (TATP). *Sensors* **2014**, *14*, 23269–23282. doi:10.3390/s141223269.

2. Walter, M.A.; Panne, U.; Weller, M.G. A Novel Immunoreagent for the Specific and Sensitive Detection of the Explosive Triacetone Triperoxide (TATP). *Biosensors* **2011**, *1*, 93–106. doi:10.3390/bios1030093.

3. Santos, J.P.; Fernández, M.J.; Fontecha, J.L.; Matatagui, D.; Sayago, I.; Horrillo, M.C.; Gracia, I. Nanocrystalline Tin Oxide Nanofibers Deposited by a Novel Focused Electrospinning Method. Application to the Detection of TATP Precursors. *Sensors* **2014**, *14*, 24231–24243. doi:10.3390/s141224231.

4. Lü, X.; Hao, P.; Xie, G.; Duan, J.; Gao, L.; Liu, B. A Sensor Array Realized by a Single Flexible TiO2/POMs Film to Contactless Detection of Triacetone Triperoxide. *Sensors* **2019**, *19*. doi:10.3390/s19040915.

5. Sun, Q.; Wu, Z.; Duan, H.; Jia, D. Detection of Triacetone Triperoxide (TATP) Precursors with an Array of Sensors Based on MoS2/RGO Composites. *Sensors* **2019**, *19*. doi:10.3390/s19061281.

6. Nguyen, T.T.; Phan, D.N.; Nguyen, D.C.; Do, V.T.; Bach, L.G. The Chemical Compatibility and Adhesion of Energetic Materials with Several Polymers and Binders: An Experimental Study. *Polymers* **2018**, *10*. doi:10.3390/polym10121396.

7. Trofimov, V.A.; Varentsova, S.A. A Possible Way for the Detection and Identification of Dangerous Substances in Ternary Mixtures Using THz Pulsed Spectroscopy. *Sensors* **2019**, *19*. doi:10.3390/s19102365.

8. Manley, P.V.; Sagan, V.; Fritschi, F.B.; Burken, J.G. Remote Sensing of Explosives-Induced Stress in Plants: Hyperspectral Imaging Analysis for Remote Detection of Unexploded Threats. *Remote Sensing* **2019**, *11*. doi:10.3390/rs11151827.

9. Herrera-Chacon, A.; Campos, I.; Bottone, L.; Valle, M.d. Molecularly Imprinted Polymers for TNT Analogues. Development of Electrochemical TNT Biosensors. *Proceedings* **2017**, *1*. doi:10.3390/proceedings1080731.

10. Charles, P.T.; Wadhwa, V.; Kouyate, A.; Mesa-Donado, K.J.; Adams, A.A.; Deschamps, J.R.; Kusterbeck, A.W. A High Aspect Ratio Bifurcated 128-Microchannel Microfluidic Device for Environmental Monitoring of Explosives. *Sensors* **2018**, *18*. doi:10.3390/s18051568.

11. Marchisio, A.; Tulliani, J.M. Semiconducting Metal Oxides Nanocomposites for Enhanced Detection of Explosive Vapors. *Ceramics* **2018**, *1*, 98–119. doi:10.3390/ceramics1010009.

12. Zarejousheghani, M.; Lorenz, W.; Vanninen, P.; Alizadeh, T.; Cämmerer, M.; Borsdorf, H. Molecularly Imprinted Polymer Materials as Selective Recognition Sorbents for Explosives: A Review. *Polymers* **2019**, *11*. doi:10.3390/polym11050888.

13. Attard, G.; Barnes, C. *Surface*; Oxford Science Publications: New York, 1998.

14. Galleano, M.; Boveris, A.; Puntarulo, S. Understanding the Clausius–Clapeyron Equation by Employing an Easily Adaptable Pressure Cooker. *Journal of Chemical Education* **2008**, *85*, 276, [https://doi.org/10.1021/ed085p276]. doi:10.1021/ed085p276.

15. Sladkov, I.B.; Nedoshivina, M.S. On the accuracy of calculation by the Clapeyron-Clausius equation. *Russian Journal of Applied Chemistry* **2001**, *74*, 390–393.

16. Velasco, S.; Román, F.L.; White, J.A. On the Clausius-Clapeyron vapor pressure equation. *Journal of Chemical Education* **2009**, *86*, 106–111.

17. Yarwood, J.L.C.D.H. Vapour pressure measurements of bromine. *Vacuum* **1951**, *1*, 37–38.

18. Pikal, M.; Lukes, A. Knudsen Vapor Pressure Measurements on Pure Materials and Solutions Dispersed in Porous Media: Molded Nitroglycerin Tablets. *Journal of Pharmaceutical Sciences* **1976**, *65*, 1269 – 1277. doi:https://doi.org/10.1002/jps.2600650905.

19. Elder, J.P. Sublimation measurements of pharmaceutical compounds by isothermal thermogravivletry. *Journal of thermal analysis* **1997**, *49*, 897–905. doi:10.1007/BF01996775.

20. Jones, D.; Lightfoot, P.; Fouchard, R.; Kwok, Q. Thermal properties of DMNB, a detection agent for explosives. *Thermochimica Acta* **2002**, *388*, 159 – 173. doi:https://doi.org/10.1016/S0040-6031(02)00033-3.

21. Chatterjee, K.; Dollimore, D.; Alexander, K.S. Calculation of vapor pressure curves for hydroxy benzoic acid derivatives using thermogravimetry. *Thermochimica Acta* **2002**, *392-393*, 107 – 117. MATERIAL CHARACTERIZATION BY THERMAL ANALYSIS AND CALORIMETRY. A collection of Papers Scheduled for the 28th North American Thermal Analysis Society Conference Orlando, FL 4-6 October 2000., doi:https://doi.org/10.1016/S0040-6031(02)00091-6.

22. L. Ramirez, M.; Pacheco-Londoño, L.; Peña Quevedo, A.; Hernández-Rivera, S. Characterization of peroxide-based explosives by thermal analysis - art. no. 62012B. *Proc SPIE* **2006**, *6201*, 62012B–620111A. doi:10.1117/12.666227.

23. Stefanov, A.; Stibor, A.; Dominguez-Clarimon, A.; Arndt, M. Sublimation enthalpy of dye molecules measured using fluorescence. *The Journal of Chemical Physics* **2004**, *121*, 6935–6940, [https://doi.org/10.1063/1.1792551]. doi:10.1063/1.1792551.

24. Mehta, N.; JE, G.P.; Hernández-Rivera, S.; D, H.; Thomson, M.; PJ, M. Development of an In-Situ Spectroscopic Method for Cleaning Validation Using Mid-IR Fiber Optics. *Spectroscopy* **2003**, *18*, 14.

25. Hamilton, M.L.; Perston, B.B.; Harland, P.W.; Williamson, B.E.; Thomson, M.A.; Melling, P.J. Grazing-Angle Fiber-Optic IRRAS for in Situ Cleaning Validation. *Organic Process Research & Development* **2005**, *9*, 337–343, [https://doi.org/10.1021/op040213z]. doi:10.1021/op040213z.

26. Primera-Pedrozo, O.; Pacheco-Londono, L.; F. De la Torre-Quintana, L.; Hernández-Rivera, S.; Thomas Chamberlain, R.; T. Lareau, R. Use of fiber optic coupled FT-IR in detection of explosives on surfaces. *Proc SPIE* **2004**, *5403*, 237–245. doi:10.1117/12.542812.

27. Verdeyen, J.T. *Laser Electronics*, first ed.; Prentice-Hall, Inc: new Jersey, 1981.

28. Mansfield, E.; Kar, A.; Quinn, T.P.; Hooker, S.A. Quartz Crystal Microbalances for Microscale Thermogravimetric Analysis. *Analytical Chemistry* **2010**, *82*, 9977–9982. doi:10.1021/ac102030z.

29. Price, D.M. Volatilisation, evaporation and vapour pressure studies using a thermobalance. *Journal of Thermal Analysis and Calorimetry* **2001**, *64*, 315–322.

30. Langmuir, I. The vapor pressure of metallic tungsten. *Physical Review* **1913**, *2*, 329–342.

31. Price, D.M.; Hawkins, M. Calorimetry of two disperse dyes using thermogravimetry. *Thermochimica Acta* **1998**, *315*, 19–24.

32. Colomina, M.; Jimenez, P.; Turrion, C. Vapour pressures and enthalpies of sublimation of naphthalene and benzoic acid. *The Journal of Chemical Thermodynamics* **1982**, *14*, 779–784.

33. Ribeiro da Silva, M.A.V.; Monte, M.J.S.; Santos, L.M.N.B.F. The design, construction, and testing of a new Knudsen effusion apparatus. *The Journal of Chemical Thermodynamics* **2006**, *38*, 778–787. doi:https://doi.org/10.1016/j.jct.2005.08.013.

34. Oura, K.; Lifshits, V.G.; Saranin, A.A.; Zotov, A.V.; Katayama, M. *Surface Science: An Introduction*; Springer: Berlin Germany, 2003.

35. Redhead, P.A. Thermal desorption of gases. *Vacuum* **1962**, *12*, 203–211.

36. Tolstoy, V.P.; Chernyshova, I.V.; Skryshevsky, V.A. *Handbook of Infrared Spectroscopy of Ultrathin Films*; Wiley-Interscience: Nwe Jersey, 2003.

37. Buttigieg, G.A.; Knight, A.K.; Denson, S.; Pommier, C.; Bonner Denton, M. Characterization of the explosive triacetone triperoxide and detection by ion mobility spectrometry. *Forensic Science International* **2003**, *135*, 53–59.

38. Brauer, B.; Dubnikova, F.; Zeiri, Y.; Kosloff, R.; Gerber, R.B. Vibrational spectroscopy of triacetone triperoxide (TATP): Anharmonic fundamentals, overtones and combination bands. *Spectrochimica Acta - Part A: Molecular and Biomolecular Spectroscopy* **2008**, *71*, 1438–1445.

39. Alzate, L.F.; Ramos, C.M.; Hernandez, N.M.; Hernandez, S.P.; Mina, N. The vibrational spectroscopic signature of TNT in clay minerals. *Vibrational Spectroscopy* **2006**, *42*, 357–368.

40. Ortiz-Rivera, W.; Pacheco-Londoño, L.; Castro, J.; Felix-Rivera, H.; Hernendez-Rivera, S. Vibrational Spectroscopy Standoff Detection of Threat Chemicals. *Proc SPIE* **2011**, *8031*, 803129. doi:10.1117/12.884433.

41. Pacheco-Londoño, L.; Ortiz-Rivera, W.; Primera-Pedrozo, O.; Hernandez-Rivera, S. Vibrational spectroscopy standoff detection of explosives. *Analytical and bioanalytical chemistry* **2009**, *395*, 323–35. doi:10.1007/s00216-009-2954-y.

42. Infante-Castillo, R.; Pacheco-Londoño, L.C.; Hernandez-Rivera, S.P. Monitoring the a ® b solid-solid phase transition of RDX with Raman spectroscopy: A theoretical and experimental study. *Journal of Molecular Structure* **2010**, *970*, 51–58.

43. Infante-Castillo, R.; Pacheco-Londoño, L.; Hernandez-Rivera, S.P. Vibrational spectra and structure of RDX and its 13C- and 15N-labeled derivatives: A theoretical and experimental study. *Spectrochimica Acta - Part A: Molecular and Biomolecular Spectroscopy* **2010**, *76*, 137–141.

44. Torres, P.; Mercado, L.; Cotte, I.; Hernandez, S.P.; Mina, N.; Santana, A.; Chamberlain, R.T.; Lareau, R.; Castro, M.E. Vibrational spectroscopy study of b and a RDX deposits. *Journal of Physical Chemistry B* **2004**, *108*, 8799–8805.

45. Figueroa-Navedo, A.M.; Ruiz-Caballero, J.L.; Pacheco-Londoño, L.C.; Hernandez-Rivera, S.P. Characterization of α- and β-RDX Polymorphs in Crystalline Deposits on Stainless Steel Substrates. *Crystal Growth & Design* **2016**, *16*, 3631–3638, [https://doi.org/10.1021/acs.cgd.6b00078]. doi:10.1021/acs.cgd.6b00078.

46. Ruiz-Caballero, J.L.; Aparicio-Bolaño, J.A.; Figueroa-Navedo, A.M.; Pacheco-Londoño, L.C.; Hernandez-Rivera, S.P. Optical Properties of β-RDX Thin Films Deposited on Gold and Stainless Steel Substrates Calculated from Reflection–Absorption Infrared Spectra. *Applied Spectroscopy* **2017**, *71*, 1990–2000, [https://doi.org/10.1177/0003702817710248]. PMID: 28537428, doi:10.1177/0003702817710248.

47. Ruiz-Caballero, J.L.; Blanco-Riveiro, L.A.; Ramirez-Marrero, I.A.; Perez-Almodovar, L.A.; Colon-Mercado, A.M.; Castro-Suarez, J.R.; Pacheco-Londoño, L.C.; Hernandez-Rivera, S.P. Enhanced RDX Detection Studies on Various Types of Substrates via Tunable Quantum Cascade Laser Spectrometer Coupled with Grazing Angle Probe. *IOP Conference Series: Materials Science and Engineering* **2019**, *519*, 012007. doi:10.1088/1757-899x/519/1/012007.

48. Wold, S.; Sjöströma.; Eriksson, L. PLS-regression: A basic tool of chemometrics. *Chemometrics and Intelligent Laboratory Systems* **2001**, *58*, 109–130.

49. Mardia, J.K.V.; Kent, J.T.; Biby, J.M. *Chemometrics: Statistic and Computer Application in Analytical Chemistry*; Academic Press: London, 1980.

50. Otto, M. *Chemometrics: Statistic and Computer Application in Analytical Chemistry*; Wiley-VCH: Weinheim, 1999.

51. Brereton. *Chemometrics: Data Analysis for the Laboratory and Chemical Plant*; John Wiley & Sons, Ltd: Chichester, 2003.

52. Beebe, K.R.; Pell, R.J.; Seasholtz, M.B. *Chemometrics. A Pactricla Guide*; John Wiley & Sons, Inc: New York, 1998.

53. Primera-Pedrozo, O.; Soto-Feliciano, Y.; Pacheco-Londoño, L.; Hernandez-Rivera, S. Detection of High Explosives Using Reflection Absorption Infrared Spectroscopy with Fiber Coupled Grazing Angle Probe/FTIR. *Sensing and Imaging An International Journal* **2009**, *10*, 1–13. doi:10.1007/s11220-009-0042-1.

54. Primera-Pedrozo, O.; Soto-Feliciano, Y.; Pacheco-Londoño, L.; Hernandez-Rivera, S. High Explosives Mixtures Detection Using Fiber Optics Coupled: Grazing Angle Probe/Fourier Transform Reflection Absorption Infrared Spectroscopy. *Sensing and Imaging An International Journal* **2008**, *9*, 27–40. doi:10.1007/s11220-008-0041-7.

55. Galán-Freyle, N.J.; no, L.C.P.L.; Figueroa-Navedo, A.M.; Hernandez-Rivera, S.P. Standoff Detection of Highly Energetic Materials Using Laser-Induced Thermal Excitation of Infrared Emission. *Appl. Spectrosc.* **2015**, *69*, 535–544.

56. Wrable-Rose, M.; Primera-Pedrozo, O.M.; Pacheco-Londoño, L.C.; Hernandez-Rivera, S.P. Preparation of TNT, RDX and ammonium nitrate standards on gold-on-silicon surfaces by thermal inkjet technology. *Sensing and Imaging* **2010**, *11*, 147–169.

57. Thumanu, K.; Tanthanuch, W.; Lorthongpanich, C.; Heraud, P.; Parnpai, R. FTIR microspectroscopic imaging as a new tool to distinguish chemical composition of mouse blastocyst. *Journal of Molecular Structure* **2009**, *933*, 104–111.

58. Faber, N.M.; Bro, R. Standard error of prediction for multiway PLS-1. Background and a simulation study. *Chemometrics and Intelligent Laboratory Systems* **2002**, *61*, 133–149.

59. Felipe-Sotelo, M.; Cal-Prieto, M.J.; J., F.; Boque, R.; Andrade, J.M.; Carlosena, A. Linear PLS regression to cope with interferences of major concomitants in the determination of antimony by ETAAS. *Journal of Analytical Atomic Spectrometry* **2006**, *21*, 61–68.

60. Galan-Freyle, N.J.; Pacheco-Londoño, L.C.; Roman-Ospino, A.D.; Hernandez-Rivera, S.P. Applications of Quantum Cascade Laser Spectroscopy in the Analysis of Pharmaceutical Formulations. *Applied Spectroscopy* **2016**, *70*, 1511–1519, [https://doi.org/10.1177/0003702816662609]. PMID: 27558366, doi:10.1177/0003702816662609.

61. Pacheco-Londoño, L.C.; Aparicio-Bolaño, J.A.; Galan-Freyle, N.J.; Roman-Ospino, A.D.; Ruiz-Caballero, J.L.; Hernandez-Rivera, S.P. Classical Least Squares-Assisted Mid-Infrared (MIR) Laser Spectroscopy Detection of High Explosives on Fabrics. *Applied Spectroscopy* **2019**, *73*, 17–29, [https://doi.org/10.1177/0003702818780414]. PMID: 29767535, doi:10.1177/0003702818780414.

62. IUPAC. Erratum: International union of pure and applied chemistry analytical chemistry division commission on spectrochemical and other optical procedures for analysis nomenclature, symbols, units and their usage in spectrochemical analysis - II. Data interpretation (Analytical Chemistry (1976) 48 (1424)). *Analytical Chemistry* **1976**, *48*, 2293.

63. Goldberg, I.G.; Swift, J.A. New Insights into the Metastable β Form of RDX. *Crystal Growth & Design* **2012**, *12*, 1040–1045. doi:10.1021/cg201718a.

64. Verevkin, S.P. Enthalpy of sublimation of dibenzofuran: a redetermination. *Physical Chemistry Chemical Physics* **2003**, *5*, 710–712. doi:10.1039/B208228D.

65. Bevington, P.R.; Robinson, D.K. *Data Reduction and Error Analysis for the Physical Sciences*, third ed.; McGraw-Hill: New York, 2003.

66. Hibbert, D.B. The uncertainty of a result from a linear calibration. *Analyst* **2006**, *131*, 1273–1278. doi:10.1039/B615398D.

67. Damour, P.L.; Freedman, A.; Wormhoudt, J. Knudsen Effusion Measurement of Organic Peroxide Vapor Pressures. *Propellants, Explosives, Pyrotechnics* **2010**, *35*, 514–520. doi:10.1002/prep.200900083.

68. Felix-Rivera, H.; Ramirez-Cedeño, M.L.; Sanchez-Cuprill, R.A.; Hernandez-Rivera, S.P. Triacetone triperoxide thermogravimetric study of vapor pressure and enthalpy of sublimation in 303–338 K temperature range. *Thermochimica Acta* **2011**, *514*, 37–43. doi:http://dx.doi.org/10.1016/j.tca.2010.11.034.

69. Oxley, J.C.; Smith, J.L.; Shinde, K.; Moran, J. Determination of the Vapor Density of Triacetone Triperoxide (TATP) Using a Gas Chromatography Headspace Technique. *Propellants, Explosives, Pyrotechnics* **2005**, *30*, 127–130. doi:10.1002/prep.200400094.

70. Oxley, J.C.; Smith, J.L.; Luo, W.; Brady, J. Determining the Vapor Pressures of Diacetone Diperoxide (DADP) and Hexamethylene Triperoxide Diamine (HMTD). *Propellants, Explosives, Pyrotechnics* **2009**, *34*, 539–543. doi:10.1002/prep.200800073.

71. Dunayevskiy, I.; Tsekoun, A.; Prasanna, M.; Go, R.; Patel, C.K.N. High-sensitivity detection of triacetone triperoxide (TATP) and its precursor acetone. *Applied optics* **2007**, *46*, 6397–404.

72. Espinosa-Fuentes, E.; Castro-Suarez, J.; Meza-Payares, D.; Pacheco-Londoño, L.; Hernández-Rivera, S. Sublimation enthalpy of homemade peroxide explosives using a theoretically supported non-linear equation. *Journal of Thermal Analysis and Calorimetry* **2015**, *119*, 681–688. cited By 4, doi:10.1007/s10973-014-4088-5.

73. Harris, N.J.; Lammertsma, K. Ab Initio Density Functional Computations of Conformations and Bond Dissociation Energies for Hexahydro-1,3,5-trinitro-1,3,5-triazine. *Journal of the American Chemical Society* **1997**, *119*, 6583–6589. doi:10.1021/ja970392i.

74. Rice, B.M.; Chabalowski, C.F. Ab Initio and Nonlocal Density Functional Study of 1,3,5-Trinitro-s-triazine (RDX) Conformers. *The Journal of Physical Chemistry A* **1997**, *101*, 8720–8726. doi:10.1021/jp972062q.

75. Vladimiroff, T.; Rice, B.M. Reinvestigation of the Gas-Phase Structure of RDX Using Density Functional Theory Predictions of Electron-Scattering Intensities. *The Journal of Physical Chemistry A* **2002**, *106*, 10437–10443. doi:10.1021/jp021450b.

76. Lenchitz, C.; Velicky, R.W. Vapor pressure and heat of sublimation of three nitrotoluenes. *Journal of Chemical and Engineering Data* **1970**, *15*, 401–403. doi:10.1021/je60046a022.

77. Pella, P.A. Generator for producing trace vapor concentrations of 2,4,6-trinitrotoluene, 2,4-dinitrotoluene, and ethylene glycol dinitrate for calibrating explosives vapor detectors. *Analytical Chemistry* **1976**, *48*, 1632–1637. doi:10.1021/ac50005a054.

78. Lenchitz, C.; Velicky, R.W.; Silvestro, G.; Schlosberg, L.P. Thermodynamic properties of several nitrotoluenes. *The Journal of Chemical Thermodynamics* **1971**, *3*, 689–692. doi:http://dx.doi.org/10.1016/S0021-9614(71)80090-3.

79. Edwards, G. The vapour pressure of 2 : 4 : 6-trinitrotoluene. *Transactions of the Faraday Society* **1950**, *46*, 423–427. doi:10.1039/TF9504600423.

80. Dionne, B.C.; Rounbehler, D.P.; Achter, E.K.; Hobbs, J.R.; Fine, D.H. Vapor pressure of explosives. *Journal of Energetic Materials* **1986**, *4*, 447–472. doi:10.1080/07370658608011353.

81. Gershanik, A.P.; Zeiri, Y. Sublimation Rate of TNT Microcrystals in Air. *The Journal of Physical Chemistry A* **2010**, *114*, 12403–12410. doi:10.1021/jp105168h.

82. Eiceman, G.A.; Preston, D.; Tiano, G.; Rodriguez, J.; Parmeter, J.E. Quantitative calibration of vapor levels of TNT, RDX, and PETN using a diffusion generator with gravimetry and ion mobility spectrometry. *Talanta* **1997**, *45*, 57–74. doi:http://dx.doi.org/10.1016/S0039-9140(97)00107-0.

83. Leggett, D.C. Vapor pressure of 2,4,6-trinitrotoluene by a gas chromatographic headspace technique. *Journal of Chromatography A* **1977**, *133*, 83–90. doi:http://dx.doi.org/10.1016/S0021-9673(00)89207-9.

84. Hikal, W.M.; Weeks, B.L. Sublimation kinetics and diffusion coefficients of TNT, PETN, and RDX in air by thermogravimetry. *Talanta* **2014**, *125*, 24–28. doi:http://dx.doi.org/10.1016/j.talanta.2014.02.074.

85. Hikal, W.M.; Paden, J.T.; Weeks, B.L. Thermo-optical determination of vapor pressures of TNT and RDX nanofilms. *Talanta* **2011**, *87*, 290–294. doi:http://dx.doi.org/10.1016/j.talanta.2011.10.020.

86. Mu, R.; Ueda, A.; Liu, Y.C.; Wu, M.; Henderson, D.O.; Lareau, R.T.; Chamberlain, R.T. Effects of interfacial interaction potential on the sublimation rates of TNT films on a silica surface examined by QCM and AFM techniques. *Surface Science* **2003**, *530*, L293–L296. doi:http://dx.doi.org/10.1016/S0039-6028(03)00380-7.

87. Chickos, J.S.; Acree, W.E.   Enthalpies of Sublimation of Organic and Organometallic Compounds. 1910–2001.   *Journal of Physical and Chemical Reference Data* **2002**, *31*, 537–698. doi:doi:http://dx.doi.org/10.1063/1.1475333.

88. Cundall, R.B.; Frank Palmer, T.; Wood, C.E.C. Vapour pressure measurements on some organic high explosives. *Journal of the Chemical Society, Faraday Transactions 1: Physical Chemistry in Condensed Phases* **1978**, *74*, 1339–1345. doi:10.1039/F19787401339.

89. Pella, P.A. Measurement of the vapor pressures of tnt, 2,4-dnt, 2,6-dnt, and egdn. *The Journal of Chemical Thermodynamics* **1977**, *9*, 301–305. doi:http://dx.doi.org/10.1016/0021-9614(77)90049-0.

90. Jones, A.H. Sublimation Pressure Data for Organic Compounds. *Journal of Chemical and Engineering Data* **1960**, *5*, 196–200. doi:10.1021/je60006a019.

91. Hikal, W.M.; Weeks, B.L. Non-Isothermal Sublimation Kinetics of 2,4,6-Trinitrotoluene (TNT) Nanofilms. *Molecules* **2019**, *24*. doi:10.3390/molecules24061163.

92. Lee, Y.J.; Weeks, B.L. Investigation of Size-Dependent Sublimation Kinetics of 2,4,6-Trinitrotoluene (TNT) Micro-Islands Using In Situ Atomic Force Microscopy. *Molecules* **2019**, *24*. doi:10.3390/molecules24101895.

93. Rosen, J.M.; Dickinson, C. Vapor pressures and heats of sublimation of some high-melting organic explosives. *Journal of Chemical and Engineering Data* **1969**, *14*, 120–124.

94. Gershanik, A.P.; Zeiri, Y. Sublimation Rate of Energetic Materials in Air: RDX and PETN. *Propellants, Explosives, Pyrotechnics* **2012**, *37*, 207–214. doi:10.1002/prep.201100038.

Sample Availability: Samples of the compounds ...... are available from the authors.